EO Africa // ARIES

D07_ATBD_PS_I

– ATBD/s and Product Specification

Version 2.0, May 2024

Contract No: 4000139191/22/I-DT

submitted by

	VISTA Remote Sensing in Geosciences GmbH (VISTA)
	Vlaamse Instelling voor Technologisch Onderzoek, Naamloze vennootschap (VITO)
	Luxemburg Institute of Science and Technology (LIST)

ESA STUDY CONTRACT REPORT

ESA Contract No 4000139191/22/I-DT	SUBJECT EO Africa // ARIES		CONTRACTOR VISTA Remote Sensing in Geosciences GmbH (VISTA)
* ESA CR( )No	* STAR CODE	Vol.1	* ESA CR( )No

ABSTRACT:
This document describes the algorithms developed within ARIES and further specifies the developed products. Version 2.0 Status: 02. May 2024
The work described in this report was done under ESA Contract. Responsibility for the contents resides in the author or organisation that prepared it.
Names of authors: Veronika Otto (Vista), Silke Migdall (Vista), Jeroen Degerickx (Vito), Louis Snyders (Vito), Kanishka Mallick (LIST), Aolin Jia (List)

** NAME OF ESA STUDY MANAGER Mr. Z. Szantoi DIV: EOP-SDR DIRECTORATE: Earth Observation Programmes	** ESA BUDGET HEADING

Authors of report

The present report was prepared by:

Veronika Otto, Silke Migdall
VISTA Geowissenschaftliche Fernerkundung GmbH
Gabelsbergerstr. 51, D-80333 Munich, Germany

Jeroen Degerickx, Louis Snyders
Vlaamse Instelling voor Technologisch Onderzoek, Naamloze vennootschap
(VITO)

Kanishka Mallick, Aolin Jia
Luxembourg Institute of Science and Technology (LIST)

Content

Figures

Tables

List of Acronyms

ALIA	Average Leaf Angle
AOI	Area of Interest
ASI	Agenzia Spaziale Italiana
CC	Correlation Coefficient
CWC	Canopy Water Content
DEM	Digital Elevation Model
DLR	German Aerospace Center
DMS	Data Mining Sharpener
ECOSTRESS	ECOsystem Spaceborne Thermal Radiometer Experiment on Space Station
EnMAP	Environmental Mapping and Analysis Program
ERA	European Centre for Medium-Range Weather Forecasts atmospheric reanalysis
ESI	Evaporative Stress Index
ET	Evapotranspiration
ET0	Reference Evapotranspiration
HR	High-Resolution
ISMN	International Soil Moisture Network
ISS	International Space Station
KBDI	Keetch-Byram Drought Index
LAI	Leaf Area Index
LiDAR	Light Detection and Ranging
LST	Land Surface Temperature
LUT	Look-up Table
LWC	Leaf Water Content
MODIS	Moderate Resolution Imaging Spectroradiometer
MW	Microwave
NASA	National Aeronautics and Space Administration
NDVI	Normalized Difference Vegetation Index
NDWI	Normalized Difference Water Index
RMS	Root-Mean-Square
RS	Remote Sensing
PRISMA	PRecursore IperSpettrale della Missione Applicativa
PWC	Plant Water Concentration
PWR	Plant Water Retrieval
S2	Sentinel-2
S3	Sentinel-3
SDCI	hybrid Scaled Drought Condition Index
SLSTR	Sea and Land Surface Temperature Radiometer
SMAP	Soil Moisture Active Passive
STD	Standard Deviation
STR	Shortwave Infrared Transformed Reflectance
SW	Split-Window
SWI	Soil Water Index
SWIR	Shortwave Infrared
TIR	Thermal Infrared
WI	Water Index
*	Cross-calibrated

Introduction

This document describes the theoretical algorithm baseline for the deduction of the drought and water parameters developed in ARIES. The scientific and mathematical theory behind the algorithms is detailed, so that users can gain an informed understanding of the technical and scientific considerations underlying the products, ranging from the scientific description to mathematical definitions of the algorithms as well as references to literature underpinning the performance of these algorithms.

The following algorithms are described:

- Thermal Algorithms:

    o Drought Index and comparable products

    o High-resolution crop water stress (20m)

- Hyperspectral Algorithms:

    o Leaf Area Index Derivation via radiative transfer model inversion

    o Leaf Water Derivation via radiative transfer model inversion

    o Plant Water Retrieval via dedicated plant water absorption index

1 Thermal Data Products

1.1 Drought Index

Drought is characterized by a prolonged deficiency in water supply, affecting various aspects such as the atmosphere, soil, streamflow, groundwater, and economic activities (AghaKouchak et al., 2015). It poses substantial challenges to socioeconomic systems, leading to issues like food security, water resource inequality, and environmental degradation, including desertification and debris flow. Africa emerges as a focal point for drought-induced global change, with frequent hazards adversely affecting biodiversity and natural resource sustainability (Hadebe et al., 2017). The increasing frequency of drought exacerbates these

challenges, resulting in tropical wildfires, heatwaves, and affecting approximately 20% of the population with hunger (Otekunrin et al., 2020). Urgent efforts are needed for effective drought monitoring in Africa. Diverse drought indices, reliant on meteorological variables and remote sensing (RS) data, have been developed.

Regional applicability of meteorological drought indices faces challenges due to the limited coverage of ground-based monitoring stations. In comparison, satellite RS offers a promising alternative by leveraging indirect indicators such as green vegetation dynamics and land surface temperature (LST) variations. Nevertheless, RS-based indices encounter limitations such as infrequent temporal sampling and cloud cover (Jia et al., 2022). Furthermore, they often lack clear physical interpretations essential for effective water resource management and policy development. Soil moisture RS products are available on a daily basis, whereas they are constrained by coarse spatial resolutions (> 9 km), restricting their effectiveness for localized irrigation planning. Additionally, the validation of existing drought indices, remains insufficient across diverse landscapes and climatic conditions in Africa. Addressing these gaps is crucial for enhancing the reliability and applicability of drought monitoring systems across the region.

Therefore, developing drought indices that incorporate thermal and optical data from advanced remote sensing (RS) sensors will significantly improve our ability to monitor agricultural drought at the local level. The ECOsystem Spaceborne Thermal Radiometer Experiment on Space Station (ECOSTRESS) was deployed aboard the International Space Station (ISS) on June 29, 2018 (Fisher et al., 2020). It Serves as a pioneering mission for forthcoming Thermal Infrared (TIR) endeavors, capturing thermal imagery across five bands spanning 8 to 12.5 μm. With its advanced capabilities, it achieves high spatio-temporal resolution, obtaining TIR data at various times throughout the day. Through resampling at the nadir, ECOSTRESS achieves a pixel size of approximately 70 × 70 m, facilitating the retrieval of evapotranspiration (ET) data at fine spatial scales, including small ecosystem patches and individual agricultural fields. The revisit time averages between 1 to 5 days, significantly surpassing previous high resolution thermal missions (e.g., Landsat). In regions with high latitude where the ISS orbital path varies, observation frequency can increase, allowing multiple observations within a single day. This frequent observation capability is particularly advantageous for assessing agricultural heat and

water stress (Jia et al., 2024). Therefore, within this project, thermal drought indices will be utilized using ECOSTRESS data alongside other high-resolution optical data across Africa.

1.1.1 Algorithm Overview

Evaporative Stress Index (ESI), calculated based on ECOsystem Spaceborne Thermal Radiometer Experiment on Space Station (ECOSTRESS) evapotranspiration product, is proposed as the primary thermal drought index in the project. In addition, several meteorological and agricultural drought indices are employed for the evaluation and inter-comparison.

The Keetch-Byram Drought Index (KBDI), calculated using maximum daily temperature and total daily precipitation from the fifth-generation European Centre for Medium-Range Weather Forecasts atmospheric reanalysis v5 (ERA5), serves as a meteorological drought index. Shortwave Infrared Transformed Reflectance (STR), derived from Moderate Resolution Imaging Spectroradiometer (MODIS) shortwave infrared reflectance sensitive to water content, is used as a representative RS-based index. Additionally, a hybrid Scaled Drought Condition Index (SDCI) is involved, calculated using normalized MODIS LST, Normalized Difference Vegetation Index (NDVI), and precipitation from ERA5. To better validate the drought indices, in-situ SM from 36 sites within the International Soil Moisture Network (ISMN) in Africa serves as the ground truth for agricultural drought signals. The drought indices were implemented at 8-day and monthly scales.

1.1.2 Algorithm Description

1.1.2.1 Scientific Theory

The ECOSTRESS mission delivers the ET product globally and in near real-time.. ET encompasses the combined processes of water vapor evaporation from various surfaces of the Earth, including soil and plant surfaces, as well as transpiration from plants, representing the total water loss from the Earth's land surface to the atmosphere. It plays a pivotal role in the water cycle, influencing both regional and global climate patterns, as well as agricultural productivity and water resource management. Reference Evapotranspiration (ET0) indicates

the potential evapotranspiration under optimal surface wetness conditions. The Evaporative Stress Index (ESI), computed as the ratio of ET to ET0, serves as a widely used agricultural drought index, highlighting areas with anomalously high or low rates of water use.

The KBDI is a widely used drought index (Alexander, 1990) for assessing fire potential in forested or grassland areas. Developed by John Keetch and George Byram in the 1960s, KBDI integrates rainfall and soil moisture data over a specific period to quantify the dryness of the soil. It is based on the premise that the drier the soil, the more susceptible it is to ignition and rapid spread of wildfires. KBDI values range from 0 to 800 or higher, with higher values indicating drier conditions and increased fire danger. KBDI is valuable for wildfire management agencies, land managers, and policymakers to assess fire risk and allocate resources for fire prevention and suppression efforts.

STR is an effective drought index derived from the shortwave infrared (SWIR) bands (Yue et al., 2019). STR is particularly sensitive to variations in surface water content, making it a valuable tool for monitoring changes in soil moisture levels, vegetation health, and hydrological processes. This information is crucial for various applications, including drought monitoring, agricultural management, and water resource assessment.

The Hybrid Scaled Drought Condition Index (SDCI) (Rhee et al., 2010) is a comprehensive metric used for assessing drought conditions by integrating multiple environmental variables. Normalized LST provides insights into surface temperature variations, which can indicate drought stress in vegetation and soil moisture levels. NDVI, on the other hand, measures the health and vigor of vegetation, offering an indication of vegetation response to moisture availability. Finally, precipitation data from ERA5 captures the actual amount of rainfall, a critical factor in assessing drought severity. By combining these variables into a single index, the SDCI offers a holistic view of drought conditions, considering both temperature-driven stress and vegetation response alongside precipitation deficits. This hybrid approach enhances the accuracy and reliability of drought monitoring, enabling stakeholders to better understand and manage drought impacts on ecosystems, agriculture, and water resources.

1.1.2.2 Mathematical Theory

The equation for ESI calculation is represented mathematically as Eq. 1:

$$ESI = \frac{ET}{ET_0}, (1)$$

where ET represents the evapotranspiration, ET_0 is the reference evapotranspiration.

The KBDI (Brown et al., 2021), initially designed for daily fire risk monitoring, is calculated using normal annual precipitation, daily maximum air temperature, and daily precipitation. Some studies considered it as an indicator of surface moisture deficient in their analysis. It is based on water balance theory, ranging from 0 to 800 (0.01 inches, using English units) or 0 to 203.2 (mm, using S.I. units), representing the spectrum from wet to dry conditions. The computation process to obtain KBDI (Q) is represented as:

$$dQ = \frac{[203.2-Q][0.968\exp(0.0875T+1.5552)-8.30]d\tau}{1+10.88\exp(-0.001736R)}, (2)$$

$$Q = Q_0 + dQ - dP, (3)$$

where dQ represents drought incremental rate that is used for updating KBDI (Q_0) of the previous day, T is daily maximum air temperature, R is mean annual precipitation, dP is daily precipitation, $d\tau$ denotes the time increment set to 1 day in this study. The daily KBDI is averaged to 8-day/monthly for sensitivity evaluation. Note that $dQ = 0$ when T < 10°C, and only the dP is considered when it exceeds the net accumulated precipitation of 5 mm.

STR is calculated based on shortwave infrared reflectance (RSWIR) that is sensitive to surface water content:

$$STR = \frac{(1-R_{SWIR})^2}{2R_{SWIR}}, (4)$$

Subsequently, to obtain the scaled STR as a drought index, STR is detrended to remove seasonal cycles by the wettest (highest STR) and driest (lowest STR) values in the historical records at the same month/day of year.

By using the anomaly information of precipitation (P), LST, and NDVI, we will develop SDCI as follows:

$$SDCI = 0.5\,PCI + 0.25\,VCI + 0.25\,TCI, \text{ (5)}$$

$$TCI = \frac{LST_{max} - LST_i}{LST_{max} - LST_{min}}, \text{ (6)}$$

$$PCI = \frac{P_i - P_{min}}{P_{max} - P_{min}}, \text{ (7)}$$

$$VCI = \frac{NDVI_i - NDVI_{min}}{NDVI_{max} - NDVI_{min}}, \text{ (8)}$$

where PCI (precipitation condition index), VCI (vegetation condition index), and TCI (temperature condition index) in Eqs. (2-5) represent detrended results from monthly or 8-days values of P, LST, and NDVI. The SDCI is the weighted average of the three indices and the weights are pre-determined based on previous studies.

1.1.2.3 Algorithm Input and Output Variables

The ECOSTRESS ESI output is operated by NASA Jet Propulsion Laboratory (JPL), and the ET product is estimated based on the 70-m resolution level-3 ECOSTRESS LST product, thus ESI is considered as the level-4 output in the product list. The ECOSTRESS ESI is generated globally and freely available online in near real time. Other released indices require input variables listed below.

Table 1: Algorithm input and output variables

Drought Index	Input Variable	Input Data
KBDI	Daily maximum air temperature	ERA5-Land
	Daily precipitation	ERA5-Land
STR	SWIR band (2105–2155 nm)	MODIS
SDCI	Daily precipitation	ERA5-Land
	Daily NDVI	MODIS
	Daily LST	MODIS

1.1.3 Algorithm Usage Constraints

The present ECOSTRESS ESI is computed based on clear-sky LST data. While it effectively reveals intricate spatial patterns for mapping drought at local scales, its utility is significantly compromised by cloud cover. Additionally, the lack of a fixed revisit time throughout the day results in temporally adjacent ESI images. This variability may render them not directly comparable, as the ESI exhibits a distinct diurnal cycle. Consequently, while the current clear-sky ESI output serves as a valuable tool for mapping drought stress, its capability to capture temporal variability in drought conditions is limited. Therefore, there exists a potential gap in effectively monitoring drought temporal dynamics over time using the current ESI product. Additionally, all RS-based drought indices currently face challenges due to cloud cover. Therefore, to enhance the applicability of the algorithms, it is advisable to concentrate on an 8-day or monthly scale.

1.1.4 Performance Assessment

1.1.4.1 Validation Methods

The ISMN functions as a centralized repository for globally accessible (Al-Yaari et al., 2019), in situ soil moisture measurements. It systematically aggregates, standardizes, and openly disseminates in-situ soil moisture data obtained at various depths across diverse networks. Soil moisture is considered as the indicator of agricultural drought as agricultural drought is generally defined as the soil water deficit that impacts the crop yield. In this project, we employed surface soil moisture measurements obtained from 36 ground sites in Africa, covering a spectrum of climate and land cover types. The correlation coefficient will be computed between in-situ soil moisture and various drought indices to assess their effectiveness in capturing ground surface wetness across diverse climate and biome conditions. Additionally, following seasonality detrending, comparisons will be made between soil moisture anomalies and detrended drought indices to determine the indices' ability to capture soil moisture deficits.

1.1.4.2 Uncertainties

The statistics of correlation coefficient between soil moisture with drought indices at 8-day and monthly scales have been summarized in Table 2.

Table 2: Median value at different sites and overall standard deviation (STD) statistics of Correlation coefficient (cc) between in-situ SM and different drought indices at 8-day and monthly scales.

Index	8-day		monthly	
	cc	STD	cc	STD
KBDI	-0.47	0.17	-0.55	0.24
SDCI	0.40	0.15	0.44	0.24
STR	0.60	0.21	0.61	0.25
ESI	0.49	0.16	0.53	0.19

More detailed validation and comparison are provided in the validation report.

1.1.5 Algorithm Implementation

The ECOSTRESS ESI and MODIS products are free available at NASA Earthdata. The access is https://search.earthdata.nasa.gov/search?q=C1534730762-LPDAAC_ECS. In addition, NASA also provides an online sampling tool that allows end users to directly sample the products based on uploaded site geo-locations and shapefiles of the region of interest for their study. The online sampling tool is available at https://appeears.earthdatacloud.nasa.gov/.

The ERA5-Land is available at https://cds.climate.copernicus.eu/cdsapp#!/dataset/reanalysis-era5-land?tab=overview and Google Earth Engine (https://earthengine.google.com/).

1.1.6 Significance Discussion

The ECOSTRESS ESI is the first operational thermal drought index that is available at 70 m spatial resolution. It provides the promising ability to monitor evaporative stress across diverse regions and ecosystems in Africa. With the availability of near real-time or regularly updated data, the 70-m ESI can provide timely insights into changing drought conditions, allowing for prompt interventions and adaptive responses to mitigate the impacts of drought on agriculture,

water supplies, and ecosystems. The availability of high-resolution global ESI data opens up new opportunities for research and innovation in drought monitoring, climate studies, agricultural modeling, and water resource management. Researchers can use this dataset to develop and validate new algorithms, improve drought forecasting models, and advance our understanding of the complex interactions between climate, land surface processes, and water availability.

In addition, the inter-comparison among drought indices driven by various input variables facilitates the interpretation of drought signals for end users. Additionally, it enables the identification of the most suitable index for specific contexts or regions.

1.1.7 Open Research

The algorithm and data processing codes will be freely available through VISTA processors.

1.2 Other drought Product

1.2.1 Data Overview

Two soil moisture RS products are included for comparison: National Aeronautics and Space Administration (NASA) Soil Moisture Active Passive (SMAP) soil moisture product (Entekhabi et al., 2010), and European Space Agency (ESA) Soil Water Index (SWI) from Copernicus Global Land Products.

1.2.2 Product Description

1.2.2.1 Scientific Theory

Two microwave (MW)-based RS soil moisture products were also included for comparison. The Soil Moisture Active Passive (SMAP) mission is a NASA satellite mission designed to measure and map global soil moisture and freeze/thaw state. The SMAP satellite carries both active and passive microwave instruments to provide high-resolution soil moisture data, enabling scientists to better understand Earth's water cycle and improve weather and climate forecasting models. The SMAP soil moisture product offers valuable insights into soil moisture dynamics at various spatial and temporal scales, aiding in

applications such as drought monitoring, flood prediction, agricultural planning, and ecosystem management.

The ESI SWI assesses soil moisture conditions at various soil depths and standardizes the measurements using historical data (Albergel et al., 2008). The SWI is calculated from Surface Soil Moisture (SSM) from Metop ASCAT sensors on both Metop-A and Metop-B using a two-layer water balance model. We incorporate them in our assessment and leverage them as references for large-scale mapping purposes.

1.2.3 Algorithm Usage Constraints

The constraints of using SMAP and ESA soil moisture data to monitor agricultural drought include:

(1) Spatial and temporal resolution limitations: SMAP data may not provide sufficient spatial details to capture small-scale variations in soil moisture that are critical for agricultural drought monitoring at the field or farm level.

(2) Sensitivity to vegetation cover: SMAP measurements may be influenced by vegetation cover, leading to inaccuracies in soil moisture estimates, especially in densely vegetated areas.

(3) Limited integration with other drought indicators: SMAP soil moisture data may not be integrated effectively with other drought indicators (e.g., precipitation, temperature) to provide a comprehensive assessment of agricultural drought conditions.

1.2.4 Performance Assessment

1.2.4.1 Validation Methods

The SMAP and ESA soil moisture dataset are validated based in situ soil moisture measurements from ISMN, the same reference data that used for validating the drought indices involved in this project.

1.2.4.2 Uncertainties

The statistics of correlation coefficient between soil moisture with soil moisture products at 8-day and monthly scales have been summarized in Table 3.

Table 3: Median value at different sites and overall standard deviation (STD) statistics of Correlation coefficient (cc) between in-situ SM and different soil moisture products at 8-day and monthly scales.

Index	8-day		monthly	
	cc	**STD**	**cc**	**STD**
SMAP	0.85	0.07	0.88	0.11
SWI	0.88	0.12	0.91	0.21

1.2.5 Algorithm Implementation

The NASA SMAP soil moisture product is available at NASA earthdata (https://search.earthdata.nasa.gov/search?q=SPL4SMAU%20V007). The ESA SWI data is available at the ESA Copernicus Global Land Service platform (https://land.copernicus.eu/en/products/soil-moisture/daily-soil-water-index-global-v3-0-12-5km).

1.2.6 Significance Discussion

RS soil moisture products provide direct measurements of soil moisture content, which is a key indicator of drought conditions. Unlike some drought indices that rely on indirect measurements or proxies, the soil moisture data offer a more accurate representation of soil moisture levels in near real-time. In addition, the soil moisture products offer a sub-daily near real time gap-free soil moisture monitoring, that is suitable for temporal variability analysis of drought conditions. Thus, they capture soil moisture dynamics over time, including fluctuations in moisture levels due to precipitation events or changes in land surface conditions. This dynamic monitoring capability enhances the understanding of drought evolution and intensity, helping to assess its impacts more effectively. They can be readily incorporated into operational drought monitoring systems, providing decision-makers with timely and actionable information for drought preparedness and response. The availability of reliable soil moisture

data from SMAP enhances the effectiveness of early warning systems and drought mitigation efforts.

1.2.7 Open Research

The data processing tool and code will be available through the VISTA processors.

1.3 High-resolution crop water stress (20m)

1.3.1 Algorithm Overview

The most straightforward way to derive crop water stress information from thermal Earth Observation measurements, is to compute the difference between ambient air temperature (T_{air}) and the land surface temperature (LST), as indicated by e.g. Idso et al. (1977). The general concept here is that crops having insufficient access to water resources tend to close their stomata to limit excessive water loss through transpiration. As a result, the leaf surface of the crop heats up compared to the surrounding air. Hence, strongly positive values of LST $- T_{air}$ indicate water stress in crops. Currently, the main limitation to offer such a product in an operational setting is the lack of high spatial and temporal resolution thermal satellite data. While waiting for future thermal satellite missions to bridge this gap, several data sharpening techniques have been proposed to generate high-resolution LST data based on lower resolution alternative data sources. One such popular approach is the Sen-ET algorithm, which generates 20 m daily LST data based on a data fusion approach between 1 km thermal data from Sentinel-3 (S3) and 20 m optical data from Sentinel-2 (S2).

Three main problems can be identified regarding this sharpened 20 m LST product from Sentinel-3:

1. Generally, the operational Sentinel-3 SLSTR split-window (SW) algorithm systematically overestimates LST, due to wrongly assigned land covers and corresponding SW coefficients (Pérez-Planells et al., 2021; Sanchez et al., 2024).

2. Although the thermal sharpening procedure ensures conservation of surface energy between the low- and high-resolution products, sharpened high-resolution LST products (especially when sharpening ratios are high as is the case for S3), are known to suffer from a loss of LST dynamic contrast compared to an LST product originally

captured at high resolution. Bellvert et al. (2020) for instance concluded that extremes in LST were not properly captured in S3 sharpened LST imagery, making it less suited for precision agriculture applications as compared to high-resolution LST imagery. This is especially true for highly heterogeneous scenes such as orchards or complex agricultural landscapes in a smallholder farming context.

3. Directional effects caused by sun-sensor geometry variations between subsequent LST observations typically can result in LST differences of more than 10 K (Lagouarde & Irvine, 2008), causing important inconsistencies in LST time series.

Given these remaining issues, we suggest adding a two-stage LST correction procedure to produce higher quality high-resolution LST measurements. The first stage involves cross-calibrating the thermally sharpened LST with ECOSTRESS LST to compensate for the known quality issues with S3 data itself and the sharpening procedure. The second stage entails the quantification of directional effects by comparing simultaneous acquired cross-calibrated thermally sharpened S3 images and ECOSTRESS with different viewing geometry. This allows to remove the directional effects in the high-resolution S3 LST.

Figure 1 shows a complete overview of the process of deriving the high-resolution crop water stress product. The algorithm can be subdivided in three parts:

1. Thermal sharpening based on Sen-ET methodology.

   The thermal sharpening method is a data mining sharpener that uses S2 bands and a digital elevation model (DEM) as predictors for S3 LST (Gao et al., 2012a; Guzinski et al., 2020). The original S3 LST with a resolution of 1000 m is downscaled to S2's 20 m resolution. The resulting LST is called S3 high-resolution (HR) LST.

2. LST accuracy improvement by cross-calibration and directional corrections using ECOSTRESS data.

   During this step, the quality of the high-resolution LST product generated through S2 and S3 data fusion is improved through an additional cross-check with high-resolution (70m) LST data as obtained from ECOSTRESS. To enable a pixel-by-pixel comparison of both LST products, the S3 HR LST of 20 meter is resampled to the corresponding ECOSTRESS image. Thereafter, the process consists of two subsequent steps.

- Cross-calibration

  The direct comparison of S3 HR LST (70 m) with ECOSTRESS, excluding data with different directional effects, allows to define a gain and offset to cross-calibrate S3 HR LST to S3* HR LST.

- Directional correction

  The direct comparison of S3* HR LST (70m) with ECOSTRESS allows to retrieve directional model parameters to correct for directional effects. The correction of S3* HR LST (20 m) results in nadir S3* HR LST (20 m).

3. Crop water stress indicator retrieval.

   Based on the nadir S3* HR LST (20m) and air temperature, T_{air}, resampled to 20 meters from the hourly ERA5 dataset, the crop water stress indicator is determined. The resulting product is available twice per day (according to local Sentinel-3 overpass times).
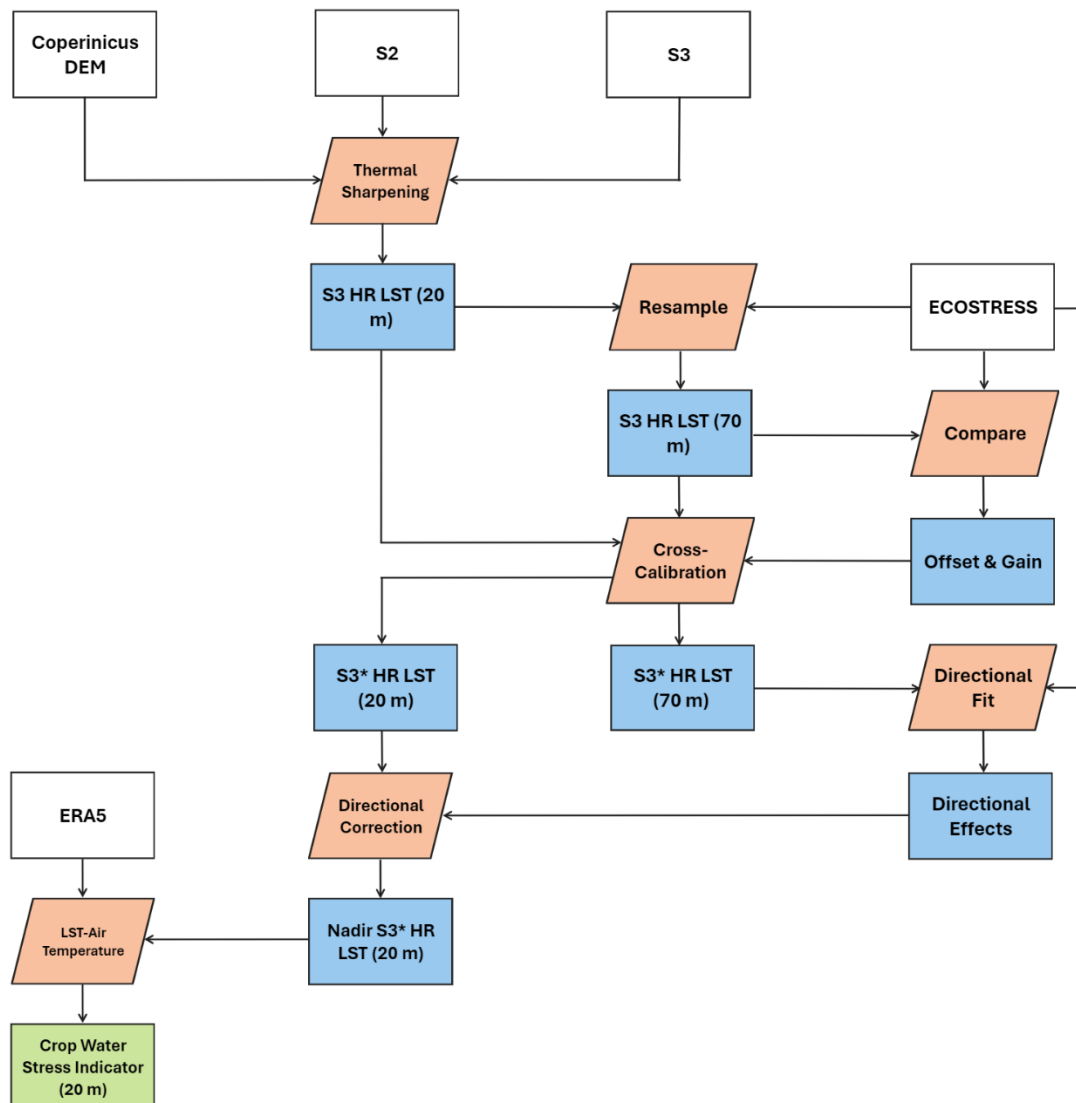
Figure 1: Algorithm overview for deriving high-resolution crop water stress indicator.

1.3.2 Algorithm Processing Steps

The following sections provide an elaborate description of the three major processing steps: thermal sharpening, cross-calibration and directional correction, and crop water stress indicator retrieval.

Thermal Sharpening

In this step, a high-resolution LST product is generated based on the fusion between high-resolution Sentinel-2 optical data and low-resolution Sentinel-3 thermal data. Each S3

acquisition is paired with a S2 acquisition, with a maximum of ten days between the two acquisitions. Then, a specific regression model, separately fitted for each S2-S3 scene pair, is employed for sharpening.

- Pre-processing steps

Based on the definition of the geographical region of interest (ROI) as well as the period of interest (start and end date) the required Sentinel-2 and Sentinel-3 imagery is downloaded. For Sentinel-2, pre-processing includes cloud masking based on the corresponding scene classification layer, 10-daily median compositing, followed by linear interpolation of any remaining data gap and finally reprojection of all bands to 20 m resolution. Based on the extent of the resulting Sentinel-2 data, the workflow reprojects and resamples the Copernicus DEM to match the S2 images. Sentinel-3 imagery is also clipped and reprojected based on the S2 tile extent. The original data is then split into an LST, a cloud mask and an observation geometry file, the latter containing information such as latitude, longitude, viewing and solar zenith and azimuth angles. These geometry variables are resampled (cubic spline interpolation) to 20 m resolution to fully match the Sentinel-2 data. As a final step, the S3 LST data is masked based on the associated cloud mask. Figure 2 shows the pre-processing flows.
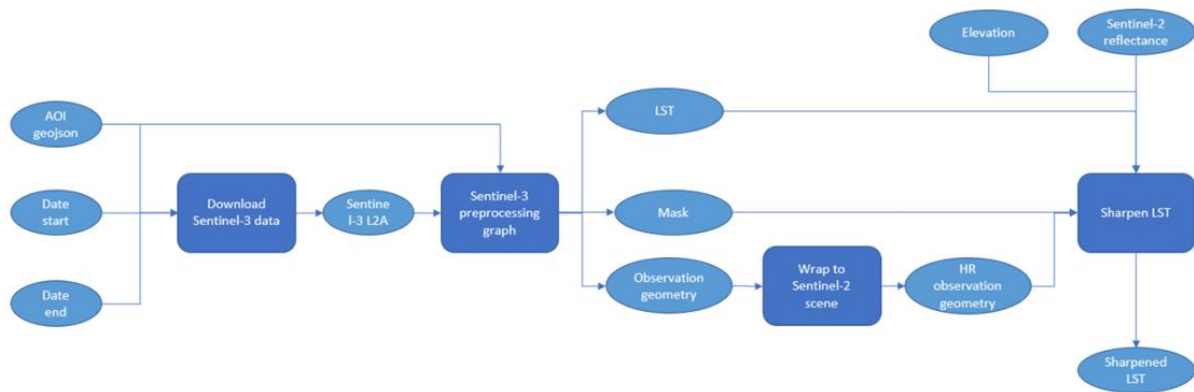

Figure 2: Pre-processing flow for Sentinel-3 data preparation. Retrieved from (USER MANUAL FOR SEN-ET SNAP PLUGIN (V1.1.0), 2020)

- Data Mining Sharpener (DMS)

Figure 3 shows the principles of the thermal data sharpening model, which is based on (Gao et al., 2012a). In essence, the method assumes a constant relation between thermal EO data

and optical EO data, irrespective of the resolution. This relation is initially established at low (S3) resolution and then applied to the high-resolution optical data to obtain sharpened thermal data. An additional bias correction between the low- and high-resolution thermal data finally ensures conservation of energy.
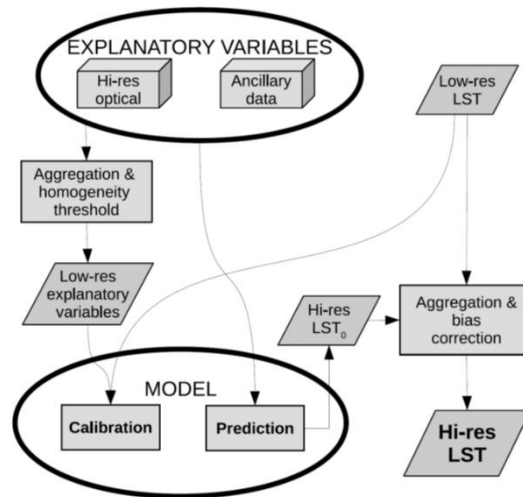
Figure 3: Thermal sharpening model. Retrieved from (Gao et al., 2012b).

The atmospherically corrected Sentinel-2 optical data, with 20 m resolution, is resampled to the corresponding SLSTR LST image, with 1 km resolution. Simultaneously, slope and aspect maps are generated from the DEM, which are resampled to SLSTR resolution, to estimate the solar irradiance incident angle for the S3 overpass time. A multivariate decision tree regression model is then trained based on the three resampled datasets and LST as the predictors and the dependent variable, respectively. The selection of training samples is automated and based on selecting 80% of non-cloudy low-resolution pixels for which the high-resolution pixels show the lowest coefficient of variation. The regression model rises as the result of a bagging ensemble of decision trees (Breiman, 1996). The decision trees are modified, such that for each leaf node the corresponding samples construct a multivariate linear model.

Unlike the original Sen-ET implementation, the decision tree sharpener is only trained on the full Sentinel-2 scene instead of using a moving window approach, to limit the processing cost of the implementation. For each observation date, a separate sharpening model is trained. In the original Sen-ET workflow, an additional bias correction has been implemented to ensure energy conservation between the original low-resolution LST and the generated high-resolution LST values. This step has been added as an optional post-processing step in our

implementation, but has been switched off by default as it generated clear artifacts in the sharpened LST products. This bias correction is achieved by comparing the emitted radiation from the predicted high-resolution LST with the original low-resolution observed LST to determine a bias. The biases serve as offsets for each low-resolution pixel. Subsequently, each offset is applied to all sharpened pixels inside the corresponding coarse pixel. The final product of the sharpening process is a 20-meter representation of the LST.

For more details related to the Sen-ET algorithm, we refer to the online manual (USER MANUAL FOR SEN-ET SNAP PLUGIN -V1.1.0, 2020).

Cross-Calibration and Directional Correction

Within this step, high-resolution LST observations from ECOSTRESS are used to improve the quality of the high-resolution LST product as derived from the combination of Sentinel-2 and Sentinel-3. The detailed procedure is explained in the following sections.

- Obtaining Quasi-Simultaneous ECOSTRESS Acquisitions

A valid inter-comparison of satellite data requires similar conditions for both datasets. Therefore, simultaneous observations are vital to avoid the introduction of temporal discrepancies. However, perfect simultaneous observations are not achievable. Hence, an assumption arises: within a specific timeframe, temperature changes are negligible. Existing guidelines on LST validation/intercomparison suggest dology to select observations maximally 10 minutes before or after the acquisition of S3 (Guillevic et al., 2018):

> *For LST product intercomparisons, we recommend to select data with view angles lower than 45°, a satellite angular separation limit of ±10° and a satellite time separation limit of ±10 minutes.*

Although minor temporal effects may exist, merging extensive datasets with random minor heating and cooling effects diminishes the influence of these effects in the overall data analysis. Note that due to the presence of directionality effects only observation pairs with similar viewing geometry are selected from the quasi-simultaneous observations for this cross-sensor-calibration phase. In the next step of the procedure (see further), we will include all observation pairs again to quantify directional effects.

Here we have used ECOSTRESS LST as a cross-calibration source because of the high spatial resolution and acceptable, although irregular, temporal resolution. An alternative is

Landsat-8 LST at 100m resolution. However, the 70-meter resolution of ECOSTRESS is closer to the 20-meter resolution of the thermally sharpened LST. Furthermore, despite the irregular orbit, ECOSTRESS has a higher revisit time. NASA provides ECOSTRESS Land Surface Temperature and Emissivity (LSTE) data. Three file types for each observation combine the necessary information to extract meaningful LST data: an LSTE file, i.e., raw temperature and emissivity, a GEO file, i.e., geolocation data, and a CLOUD file, i.e., cloud cover information. The cloud file identifies cloud-covered pixels and the GEO file georeferences each pixel in the LSTE data. Note, some GEO files show in the metadata field "L1GEOMetadata/OrbitCorrectionPerformed" a False value. In that case, the georeferencing is unsuccessful for that observation, resulting in geolocation errors up to 7 km. These observations are not considered. The remaining cloud-free, i.e., cloud mask value equals zero, georeferenced LST pixels are exported as a GeoTIFF file (Figure 4).
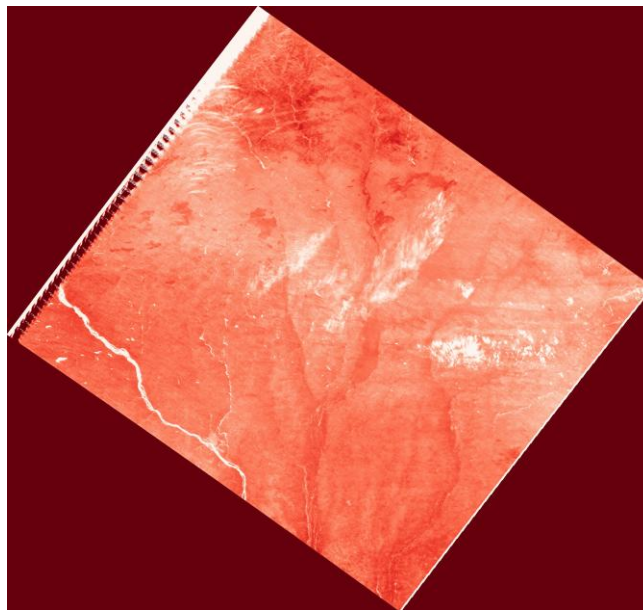
Figure 4: ECOSTRESS image.

- Reproject High-Resolution Sentinel-3 LST to ECOSTRESS image

Above, the procedure for selecting high-resolution S3 - ECOSTRESS image pairs is described. However, the downscaled S3 data has a spatial resolution of 20 meters, corresponding to the S2 data for thermal sharpening, as opposed to a spatial resolution of 70 meters for ECOSTRESS. A pixel-based comparison of two images requires pixel alignment between the two images. Therefore, in the next step, a reprojection of the S3 HR LST image to the

corresponding ECOSTRESS file, with cubic spline as the resampling method, delivers the required S3 HR LST for image comparison.

- LST inter-comparison

After high-resolution S3 resampling to ECOSTRESS, the image pair enables direct pixel-by-pixel comparison. Figure 5 shows both images and their overlapping area. This area doesn't show the absolute temperatures but the temperature difference between high-resolution S3 and ECOSTRESS, by subtracting ECOSTRESS temperatures from S3 on a pixel-basis.

The temperature difference image provides a qualitative and visual representation of how well the thermally sharpened S3 LST matches the quasi-simultaneous ECOSTRESS image. Additionally, Figure 6 provides a more quantitative representation of the image pair similarity by showing a histogram of the temperature difference of all pixels and a correlation plot of the absolute temperatures.
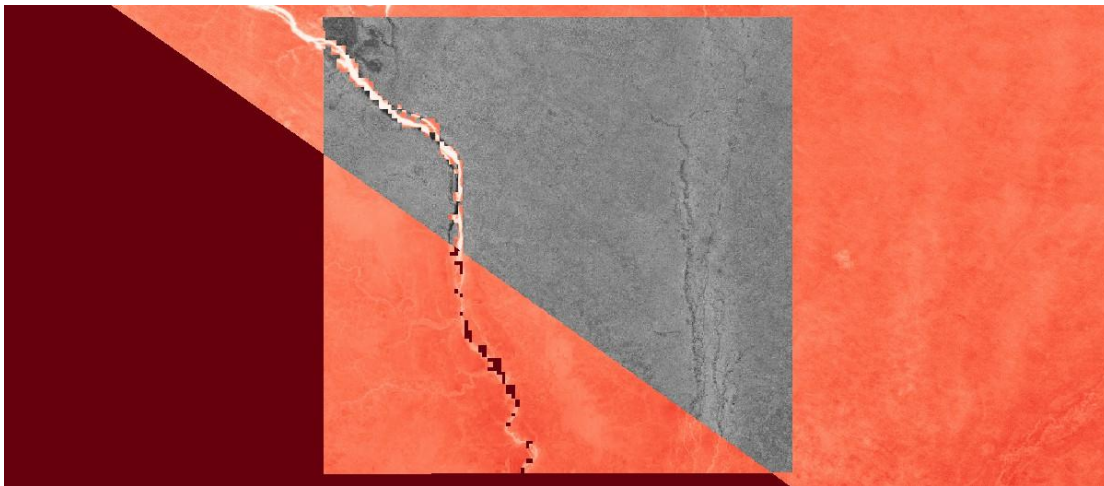
Figure 5: Intercomparison of S3 HR LST (central small square) and ECOSTRESS observation (close-up of larger tile – upper-right), both at 70-meter resolution. Their overlap is shown in grey shades as the temperature difference between S3 HR LST and ECOSTRESS LST. The figure shows the geographic region South-East of Niamey-Niger.
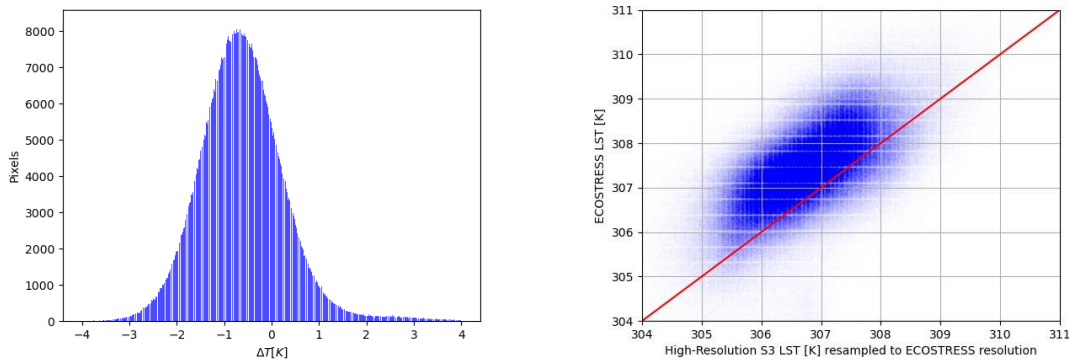
Figure 6: Histogram of temperature differences between an S3 HR LST and ECOSTRESS LST image on the left. Correlation plot of the same images on the right.

- Sampling from observation pairs

Practically, observation pairs for a specific period and region are selected in the previous steps. Instead of using all pixel pairs from each observation, a sampling procedure selects only a limited number of pixel pairs per observation, depending on the number of valid pixel pairs for that observation. There are two reasons for sampling. First, by reducing the amount of data, the necessary computational costs for determining cross-calibration coefficients and retrieving the directional model decreases. Second, the method avoids that observations containing lots of pixel pairs have a too large contribution to the final correction. Each observation receives a weight w_i based on the number of pixels n_i for that observation:

$$w_i = \frac{n_i}{10000} \qquad\qquad \text{for } n_i \leq 10000$$

$$w_i = 1 + \log\left(\frac{n_i}{10000}\right) \qquad\qquad \text{for } n_i > 10000$$

Based on the weight a sample size of s_i pixels is determined:

$$s_i = w_i \cdot 10000$$

These pixels are randomly selected and used as input for the cross-calibration and directional model determination.

- Cross-calibration

The cross-calibration of the S3-HR LST and ECOSTRESS LST aims to remove inherent differences between the two datasets. A perfect cross-calibration is based on image pairs

acquired under the same circumstances, including identical target, identical acquisition time, identical acquisition angle, etc. This means we must select quasi-simultaneous image pairs with similar acquisition angles and thus similar directional effects. We apply two rules to select pixel pairs with similar directional effects:

1. $|vza_{S3} - vza_{ECOSTRESS}| < 10°$

2. $|solar\ angle - sensor\ angle| > 10°$ for both satellites

The first rule assumes that directional effects are negligible for view zenith angles (vza) that differ less than 10°. The second rule ensures that even if the first rule applies, pixel pairs observed within the proximity of the Sun's direction are removed to avoid sharp hotspot effects, which influences an observation significantly for minor changes in acquisition angle. Based on all the pixel pairs that satisfy the requirements, a general offset and gain are determined:

$$LST_{S3,HR} = offset + gain \cdot LST_{ECOSTRESS}$$

The resulting cross-calibrated S3 HR LST then becomes:

$$LST_{S3,HR}^{*} = \frac{\left(LST_{S3,HR} - offset\right)}{gain}$$

The cross-calibration is executed on all pixels, both for the 20 m and 70 m resolution S3* HR LST. Now, we assume that the cross-calibrated datasets only differ due to directional effects.

• Directional Corrections

We assume that directional effects are invariant in time and space for a specific geographic region of interest. This assumption thus neglects the difference in directional effect for morning and evening observation or for different land covers. This approach returns a generic model, which reduces complexity and assures robustness, even for a small number of observations. The proposed approach allows for determining a single directional model for a defined area, which facilitates the implementation. However, in case of sufficient observations, a case specific directional correction is highly probable to return more accurate results.

$$LST(vza) = LST_{nadir} + A * f(vza)$$

Where LST_{nadir} is the nadir LST, A [K] represents the magnitude of directional effects and f [-] is the directional shape function, which is a function of the view zenith angle. Note that A can

be a negative value, which is often the case. In that case observed LST decreases for increasing vza. This effect is often caused by the cooler canopy covering a larger portion of the hotter soil. We choose the Vinnikov function to describe the shape of the directional effects:

$$f(vza) = 1 - \cos(vza)$$

For each pixel pair we can derive the value for A since the nadir LST is the same for both observations.

$$LST_{S3^*HR,i}\big(vza_{S3^*HR,i}\big) = LST_{nadir} + A * f(vza_{S3^*HR,i})$$

$$LST_{ECOSTRESS,i}\big(vza_{ECOSTRESS,i}\big) = LST_{nadir} + A * f(vza_{ECOSTRESS,i})$$

$$LST_{S3^*HR,i}\big(vza_{S3^*HR,i}\big) - LST_{ECOSTRESS,i}\big(vza_{ECOSTRESS,i}\big)$$
$$= A_i * \Big(f\big(vza_{S3^*HR,i}\big) - f\big(vza_{ECOSTRESS,i}\big)\Big)$$

However, single pixel pairs suffer from noise. To get a robust A value we use all pixel pairs from which only one A value is determined based on a least-squares minimization.

$$A:\ \min\left(\sum_i \left[\begin{matrix} LST_{S3^*HR,i}\big(vza_{S3^*HR,i}\big) - LST_{ECOSTRESS,i}\big(vza_{ECOSTRESS,i}\big) \\ -A * \big(f\big(vza_{S3^*HR,i}\big) - f\big(vza_{ECOSTRESS,i}\big)\big) \end{matrix} \right]^2\right)$$

Based on the retrieved A parameter, each pixel can be corrected:

$$LST_{nadir,i} = LST(vza_i) - A * f(vza_i)$$

Crop Water Stress Indicator Retrieval

Once the fully corrected LST has been generated, it is combined with air temperature data, the latter being collected from the ERA-5 hourly collection available through the Copernicus Climate Data Store. Based on the area and time period of interest, the workflow downloads the required data from the Climate Data Store (CDS). Finally, the resulting air temperature data is resampled to 20 m resolution and the correct timing is selected to match the Sentinel-3 overpass time for each individual observation.

1.3.3 Algorithm Input Variables

The algorithm requires the user to define the region of interest, specified by the S2 tile name, e.g., 31PDR, and the period of time for which the crop water stress indicator needs to be

generated. For this period and area of interest, all necessary input data for the algorithm is downloaded.

The algorithm relies mainly on data sources from Copernicus: Sentinel-2 MSI optical data, Sentinel-3 SLSTR thermal data, hourly ERA-5 reanalysis meteorological data and the 30 m Copernicus digital elevation model (DEM). Additionally, ECOSTRESS data are acquired from the WASDI platform.

1.3.4 Algorithm Output Variables

The algorithm's main output is the derived crop water stress index, expressed as a temperature difference between the land surface and the surrounding air. Additional intermediate variables, that can be considered as outputs as well, are the nadir high-resolution LST, the cross-calibration and directionality parameters. These parameters are a single gain, a single offset and a single Vinnikov parameter for the defined ROI and date range.

1.3.5 Algorithm Usage Constraints

- General constraints

The proposed algorithm makes use of optical and thermal satellite data as primary data sources. Both of these data sources are negatively affected by cloud cover. This means that in areas and periods of time characterized by heavy cloud cover, the available input data for the algorithm will be limited and drops in product quality can likely occur.

- Cross-calibration and directional corrections

The feasibility of the process of correcting the sharpened LST data depends on the availability of S3 HR LST and ECOSTRESS LST observation pairs. The more valid data pairs are found, the more accurate the correction results. The data pairs depend on the number of cloud-free ECOSTRESS observations at the time of S3 observations. The user should be aware of two limitations related to ECOSTRESS data availability:

- ECOSTRESS data is not available at latitudes higher than 52° or lower than -52° (corresponding to the maximum inclination angle of the International Space Station).

- The closer to the equator the lower the revisit frequency and thus less chance of finding a sufficient amount of observation pairs.

In general, it is recommended to check the frequency of available cloud-free observations for both Sentinel-2, Sentinel-3 and ECOSTRESS in the region and period of interest. In case data availability is a problem, the user should consider expanding either the area or period of interest to ensure sufficient data is available to produce reliable LST estimates.

1.3.6 Performance Assessment

Both the high-resolution LST product derived from Sentinel-3, Sentinel-2 and ECOSTRESS data, as well as the final crop water stress indicator have been subjected to product validation. We refer to Deliverable 6 – Validation methodology and results (D06_VM_FR_I) of the EOAfrica ARIES project for more details on the procedure and results.

1.3.7 Algorithm Implementation

1.3.7.1 Algorithm Availability

The algorithm is available as a series of Python source code files, accompanied by a Jupyter Notebook showing how to operate the workflow.

More information related to algorithm availability can be found in Deliverable 8 – Documentation of processor/toolbox/software (D08_PD_I) of the EOAfrica ARIES project.

1.3.7.2 Input Data Access

All required input data for the workflow are retrieved from the Copernicus Data Space Ecosystem (Sentinel-2, Sentinel-3, Copernicus DEM), the Copernicus Climate Data Store (ERA5) and WASDI platform (ECOSTRESS data).

1.3.7.3 Output Data Access

Final output products will be generated locally on the machine used to execute the workflow. From there, the user can upload those products to the Food Security TEP platform for proper visualization. Final outputs include a timeseries of the crop water stress indicator (LST-Ta) and the NDVI for the region and time period of interest.

1.3.8 Significance Discussion

It is important to note that the high-resolution crop water stress indicator generated here should never be interpreted on its own, but always in combination with other, more generic EO-based indicators on land cover/crop health. The crop water stress indicator purely looks at observed

land surface temperatures compared to air temperature, without considering for instance land cover or crop type information. The relation between these two temperatures is different for different land cover types (e.g. dry soil will have much higher LST compared to healthy vegetation at similar air temperatures). Abrupt changes in the indicator can be attributed to both occurrence of water stress, but also to land cover changes and/or agricultural management practices. We would hence recommend to always visualize this indicator alongside the Normalized Difference Vegetation Index (NDVI) and preferably also rainfall data to ease interpretation of the observed trends. Other data layers which could be added include a land cover and/or crop type map. Only in case of a considerable rise in the crop water stress indicator accompanied by a steady state in the NDVI, one could conclude water stress is occurring in a certain field. For convenience, the workflow also generates a 10-daily composite NDVI timeseries for the area and time period of interest.

1.3.9 Open Research

In absence of operational, high-resolution thermal missions, this algorithm makes use of 1 km Sentinel-3 LST measurements as the basis for developing a high-resolution crop water stress indicator. Converting 1 km data to 20 m data (sharpening ratio = 50) remains a challenging task, introducing a lot of uncertainty into the final product. While previous validation efforts indicate that spatial patterns are maintained in the sharpened product, the thermal contrast of thermally sharpened images remains compared to native high-resolution data. This leads to colder hot surfaces, such as a dry bare field, and hotter cold surfaces, like a wet full-grown crop field. This can significantly impact the accuracy of crop water stress indicators. Addressing this issue would enhance the overall quality of the indicator. One potential solution involves using histogram matching between quasi-simultaneous thermally sharpened Sentinel-3 (S3) and ECOSTRESS images under similar viewing conditions. This approach can help determine a transformation function that stretches thermal contrast, potentially improving the accuracy of LST estimations. This solution would replace the proposed cross-calibration procedure between both sensors, eliminating the need for gain and offset retrieval.

The approach proposed here is limited to ECOSTRESS data for correcting the sharpened S3 LST data. In the future, additional high-resolution thermal data sources could be added as well to increase the data availability for this cross-calibration procedure. This includes Landsat 8/9 data, but also future upcoming missions such as LSTM.

While general directionality corrections are effective in removing broad trends, they may prove insufficient for specific land cover or field types. Directional effects also vary depending on the time of day, since they are influenced by the temperature distribution of different scene components. Enhancing directional corrections by making them pixel and time-dependent could yield significant improvements. Separating morning and evening observations can capture more directionality, especially when the sun is present. Moreover, corelating directionality to biophysical parameters such as Normalized Difference Vegetation Index (NDVI), Leaf Area Index (LAI), and Fraction of Vegetation Cover (FCOVER) could further enhance accuracy. This requires additional research.

A final potential improvement of the algorithm lies in the directional model itself. Integrating a hotspot kernel alongside the base shape kernel can refine the model's accuracy. Currently, only the viewing angle is considered, but the Sun's position also influences observed LST. For countries at lower latitudes where the Sun reaches lower zenith angles, a hotspot correction could significantly enhance LST estimation, when the sensor's angle is close to the Sun's angle (i.e., less than 10°). For higher latitude countries, there is less need to include such an additional correction.

2 Hyperspectral Data Products

2.1 Leaf Area Index & Leaf Water Content

Leaf Area Index (LAI) is defined as the amount of leaf area (m²) in a canopy per unit ground area (m²) (Watson 1947). It is a critical variable for applications ranging from climate science to food security and agriculture as it is one of the main driving forces of net primary production, water and nutrient use, and carbon balance. As such, it is an essential variable in describing and quantifying processes such as photosynthesis, respiration, precipitation interception and carbon build-up as well as an indicator for plant health and development (Bréda 2008, GCOS 2011, Asner et al. 1998, Ballaré et al. 2012)

The Leaf Water Content (LWC) is defined as the content of water per leaf area (g/cm²). Multiplied by the leaf area, the water content of the plant can be calculated. The plant water is

an important indicator of the current status of the plant concerning its water demand and the possible need for irrigation (Quemada et al. 2021).

2.1.1 Algorithm Overview

LAI can be determined in the field through a variety of direct and indirect methods (Fang et al. 2019). Moreover, retrieving LAI from remote sensing data has been extensively studied over the last few decades (Goel 1989, Baret 2015, J. M. Chen 2018, Houborg et al. 2007, Verrelst et al. 2015, Zheng & Moskal 2009). Retrieval methods have been developed for a wide range of data captured mainly by passive multispectral, microwave and LiDAR sensors (Fang et al. 2019). More recently the developed methods, which can be categorized into empirical transfer functions and model inversion methods, are being expanded to upcoming hyperspectral sensors (Berger et al. 2018). The latter make use of a radiative transfer model, with the aim of establishing a relationship between fundamental canopy, soil and leaf properties, such as LAI, and the scene reflectance, given a specific sun-surface-sensor geometry (Goel & Thompson, 2000; S. Liang, 2004).

2.1.2 Algorithm Description

PROSAIL (Berger et al., 2018, Jacquemoud et al. 2009), which combines the PROSPECT leaf optical properties model (Jacquemoud & Baret, 1990) and the SAIL canopy bidirectional reflectance model (Verhoef, 1984) has become one of the most popular radiative transfer tools. It is generally user friendly, robust and has been consistently validated in laboratory, field and space experiments over an extended period, during which it has also been under continual development (Jacquemoud et al. 2009, Verhoef & Bach 2003, Weiss et al. 2001, Kuusk 1991, Verhoef et al. 2007, Verhoef & Bach 2007, Jacquemoud et al. 1996. Fourty et al. 1996, Le Maire et al. 2004, Feret et al. 2008, Feret et al. 2017, Feret et al. 2021). One way to apply the model is to generate a set of modelled reflectance spectra based on a set of properly configured input variables and stored in a look-up table (LUT). The subsequent inversion process determines the set of canopy biophysical variables, aiming for the best match between the calculated and the remotely sensed reflectance (D. Huang et al. 2008, Verrelst et al. 2014).

2.1.2.1 Scientific Theory

With the aim of creating an accurate LAI product based on hyperspectral data using a method that can also be used by inexperienced users, we decided to use a combination of Prospect-D and 4SAIL as integrated in the EnMAP-Box, a free an open-source plugin for QGIS (Jakimow et al. 2023). Prospect-D was chosen for its ability to simulate leaf optical properties with high accuracy through a complete plant lifecycle: from emergence, to possible stress responses, through to senescence (Feret et al. 2017). 4SAIL applies the four-stream radiative transfer modelling concept (Figure 7: Four-stream RT modelling concept as applied in Suits and SAIL models (Verhoef et al. 2007)) and is able to simulate the bi-directional reflectance of homogeneous canopies as a function of soil reflectance, illumination and viewing geometries, several structural and biophysical variables, such as LAI, average leaf angle (ALIA), and a hot spot parameter. Comprehensive descriptions of both these models have already been published in literature (Feret et al. 2017, Verhoef et al. 2007).
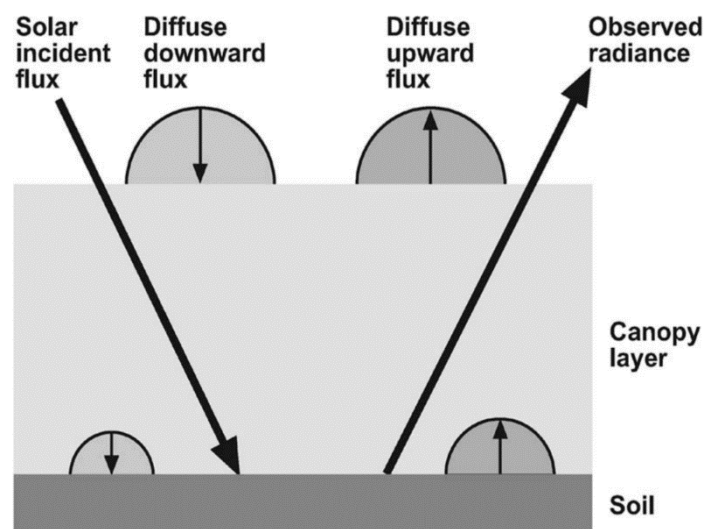

Figure 7: Four-stream RT modelling concept as applied in Suits and SAIL models (Verhoef et al. 2007)

2.1.2.2 Mathematical Theory

The mathematical theory behind radiative transfer modelling and its model inversion to derive plant parameters from reflectance spectra has been well described in the literature (Feret et al. 2017, Verhoef et al. 2007).

2.1.2.3 Algorithm Input Variables

The coupled model requires information on a relatively large number of different input variables, which are listed in Table 4.

Table 4 PROSAIL Input Variables and their Inversion status within ARIES

Parameter	Description	Unit	Model	Inversion status ARIES
N	Leaf structure parameter	-	PROSPECT	fixed
Cab	Leaf Chlorophyll a+b content	$\mu g\ cm^{-2}$	PROSPECT	Inversion (distributed)
Cw	Leaf Equivalent Water content	cm	PROSPECT	Inversion (distributed)
Cm	Leaf Mass per Area	$g\ cm^{-2}$	PROSPECT	Fixed
Ccar	Leaf Carotenoids content	$\mu g\ cm^{-2}$	PROSPECT	Fixed
Cbr	Fraction of brown leaves	-	PROSPECT	Inversion (distributed)
Canth	Leaf Anthocyanins content	$\mu g\ cm^{-2}$	PROSPECT	Fixed
LAI	Leaf Area Index	$m^2\ m^{-2}$	4SAIL	Inversion (logical)
ALIA	Average Leaf Inclination Angle	deg	4SAIL	Inversion (distributed)
Hspot	Hot Spot size parameter	-	4SAIL	Fixed
soil	Soil Reflectance (optional)	-	4SAIL	Fixed
Psoil	Soil Brightness Parameter	-	4SAIL	Fixed
SZA	Sun Zenith Angle	deg	4SAIL	Fixed

| OZA | Observer Zenith Angle | deg | 4SAIL | Fixed |
| RZA | Relative Azimuth Angle | deg | 4SAIL | Fixed |

However, neither of these do necessarily have to be available as fixed values – either spatially distributed or discreet – for the intended Area of Interest (AOI). While information on some variables is usually available (e.g. illumination and viewing geometries depend on the acquisition), other variables might be highly diverse throughout the AOI or simply unknown. The decision for fixed values versus distributed values and the way in which these values are distributed – the EnMAP toolbox application offers statistical and logical options - does however have huge consequences for the design of the LUT, which has been shown to have substantial influence on the accuracy of the inversion results (He et al. 2012). Careful LUT parametrisation paired with a sufficient size of the LUT (He et al. 2012) is thus of utmost importance.

The last column in the table shows which model parameters were fixed and which were left variable for inversion in ARIES. The size of the LUT was determined by the maximum number of possible drawings for the statistically distributed parameters available within the EnMap Toolbox, in combination with the number of steps chosen for the logically distributed parameter (LAI), resulting in a final LUT size of 710000 simulated reflectance spectra. The final parameter set used for derivation of the results can be found in the processor and toolbox description D08.

2.1.2.4 Algorithm Output Variables

The outputs of the algorithm are the variables that have been inverted in the model. In the ARIES use case, these are the leaf area index, the leaf chlorophyll a+b content, the average leaf inclination angle, the plant water content and the fraction of brown leaves. Different phenological phases can make it necessary to invert different parameters, leading to different output variables.

2.1.3 Algorithm Usage Constraints

There are mathematical constraints to the amount of variables that can be inverted, but as they are dependent on the amount of bands and hyperspectral data as 100+ bands, they are not

relevant for the ARIES case. Instead, there are computational constraints due to the large data volumes of hyperspectral data, so that the look up table size has to be carefully chosen to provide both the needed variance in the variables and computational times that can be handled. Expert knowledge of the possible ranges of the input variables is extremely helpful for this.

2.1.4 Performance Assessment

2.1.4.1 Validation Methods

The validation methods are described in detail in the Validation Document D06.

2.1.4.2 Uncertainties

Plant variables are not independent of each other, as different plant characteristics have an effect on the same parts of the spectrum. Radiative transfer modelling uses the full spectrum and physical principles to find the best approximation between the measured spectrum and a simulated spectrum to decide which plant parameters fit best. This is done using the RMS error as a criterium. Nevertheless, a perfect fit between measured and modelled spectrum is never achieved, as there are always radiometric uncertainties in the data, both from the sensor itself and from the following processing steps (e.g. geometric resampling, atmospheric correction, cirrus and haze correction), in some cases it might even be possible that a "wrong" set of parameters is chosen due to spectral similarities that are based on very different plant and canopy characteristics. Additionally, the look up table approach allows only specific steps for the inverted variables and has all other parameters fixed, leading to additional sources of error and uncertainty. The RMS error result of the model inversion is hence an important factor to assess the quality of the results. Basing the final results on multiple best solutions and adding artificial noise to account for uncertainties are established strategies to circumvent some of the mentioned sources of error (Rivera et al. 2013). These are also available in the EnMap Toolbox application.

2.1.5 Algorithm Implementation

2.1.5.1 Algorithm Availability

The algorithm is available within the EnMAP-Box, as a free and open-source plugin to QGIS, which is an open-source Geographical Information System (GIS). The two tools can be found at the following websites:

QGIS: https://qgis.org/de/site/forusers/download.html

EnMAP-Box: https://www.enmap.org/data_tools/enmapbox/

2.1.5.2 Input Data Access

The EnMAP-Box can process both PRISMA and EnMAP data. To access this data, it is necessary to write a short tender to ASI and DLR respectively, as the data is only available for research purposes and cannot be shared. More details on data access can be found here:

PRISMA: https://www.asi.it/en/earth-science/prisma/

EnMAP: https://www.enmap.org/data_access/

The other input data to the model comprise of leaf, canopy, soil and geometric parameters. The geometric parameters are the viewing angles defined by the scene acquisition time and pointing. As of now the soil background cannot be taken directly from the scene. It is possible to use an in-situ measured soil spectrum. Leaf and canopy parameters vary with different vegetation types, default parameters are available in the toolbox.

As radiative transfer modelling is a physically based modelling approach, no training data is necessary. However, it is recommended to validate new parametrizations of vegetation in the model with in-situ data.

2.1.5.3 Output Data Access

Result data can be stored and accessed locally when using QGIS locally or it can be stored and accessed through the user account on the Food Security Explorer (https://foodsecurity-explorer.net) when using the QGIS application on the platform.

2.1.6 Significance Discussion

The significance lies first and foremost in the significance of LAI and LWC information for agricultural monitoring and decision making, the ease of application (free and open source) and the information that can be derived in combination with other variables derived from hyperspectral analysis using radiative transfer model inversion. Additionally, physically-based modelling allows to transfer the method more easily than AI models, which usually need to be trained for every new location or new time-frame.

2.1.7 Open Research

The science of radiative transfer modelling is well understood, but the parametrization for different crop types and use cases is not an easy challenge. Validation for the application of the algorithm for the African test-sites in ARIES is limited to the test-sites that have provided direct validation data. Hence, more validation of the parametrization would be beneficial. Additionally, the large number of bands in the hyperspectral data, while advantageous in terms of information content, poses a challenge in terms of computational time and memory needed for the look-up-table approach. Here, further research and development to establish new, stable methods of model inversion that allow to fully utilize the information content of the data while also being computationally efficient would be beneficial.

2.2 Canopy Water Content

Canopy water content (CWC) is a vital parameter to monitor the plant status and support a balanced water supply and irrigation. Water stored in agricultural plants is linked to biochemical factors such as vegetation transpiration (Running et al., 1991) and net primary production. Especially for agricultural management in arid regions, accurate retrieval of the water content and vegetation traits might be crucial for mitigating water stress due to climate-related droughts and heat-waves (Tagliabue et al., 2022).

2.2.1 Algorithm Overview

For canopy water retrieval from hyperspectral, it is possible to use the specific H_2O water absorption features contained in the detailed reflectance spectra. This is a difference to multi-spectral data, which significantly broader and significantly less bands and thus can only estimated the water content via broad changes in the spectrum (e.g. lower value in the short-wave infrared). Hence, where multi-spectral indices only allow for a qualitative derivation of the canopy water content, the hyperspectral absorption features allow for a quantitative derivation of the canopy water content.

2.2.2 Algorithm Description

The Plant Water Retrieval (PWR) extracts quantitative water content information in [g cm^{-2}] or [cm] from hyperspectral images. It is implemented in the EnMAP-Box (Wocher et al. 2018). It applies the Beer-Lambert law (Equation 1) to inversely determine the optical thickness d of the

water layer responsible for the water absorption feature at 970 nm using water absorption coefficients for pure liquid water.

2.2.2.1 Scientific Theory

Plant water causes specific absorption features, which can be analyzed with hyperspectral data. After calibration (see Wocher et al. 2018) the optically active water thickness d of a measured vegetation spectrum can be determined through minimization of residuals to assumed dry reflectance line.
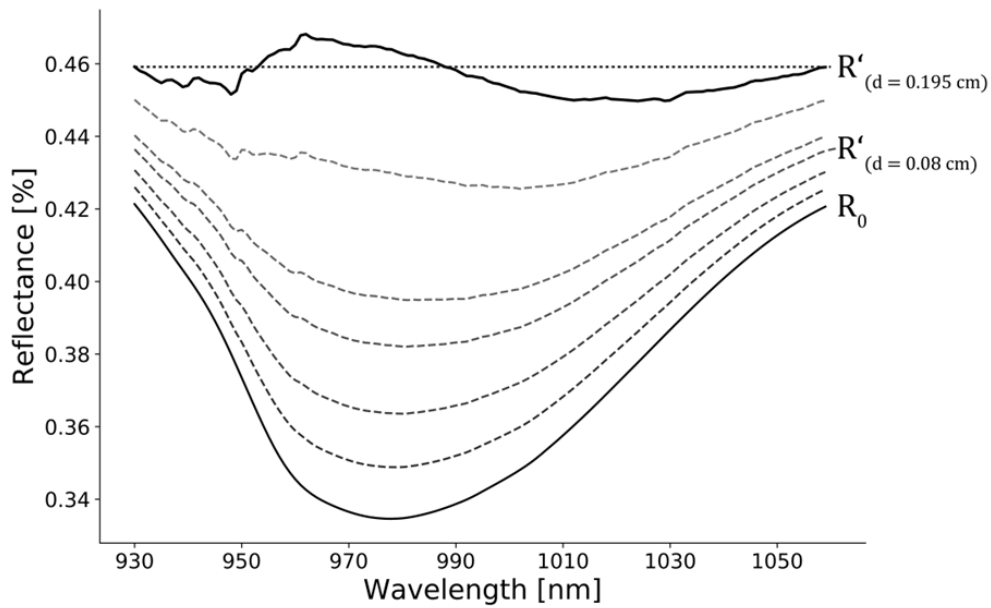

Figure 8: Determination of optically active water thickness d from a measured spectrum through minimization of residuals to assumed dry reflectance line (dotted line) (Wocher et al. 2018)

2.2.2.2 Mathematical Theory

The mathematical formulas are as follows (Wocher et al. 2018):

$$\Phi = \Phi_0 e^{-\alpha(\lambda)d}$$

$$R' = \frac{R_0}{e^{-\alpha(\lambda)d*3.52343}}$$

with R_0 being the measured reflectance. The algorithm stops when the sum of the residuals to the assumed dry reflectance is reached.

2.2.2.3 Algorithm Input Variables

Since the algorithm has already been calibrated and validated against in-situ data (Wocher et al. 2018), the only input it needs is the measured spectral reflectance of the vegetation in question.

2.2.2.4 Algorithm Output Variables

The output of the algorithm is the plant water content in [g cm^{-2}] or [cm]

2.2.3 Algorithm Usage Constraints

Some vegetation biophysical variables may disturb the signal of water: for instance, Jacquemoud, et al. (2009) noted that the leaf area index (LAI) masks the water signal between 1000 nm and 1400 nm and advised caution when using such indices for water retrieval. The comparatively low 970 nm water absorption depth is embedded in an area of generally high vegetation reflectance in the NIR. Due to the low absorption, radiation at 970 nm is expected to penetrate deeper into the canopy, reflecting a greater proportion of its total water content without a tendency to saturate. (Lillesaeter 1982, Newton & Blackman 1970, Bull 1991, Sims & Gamon 2003, Ghulam et al. 2008). Therefore, Peñuelas, et al. (1993, 1997) developed the 970 nm water index (WI) to retrieve relative plant water concentration (PWC). Other studies have also focused on 970 nm absorption for the estimation of canopy water content (Vohland 2008, Clevers et al. 2008, Clevers et al 2010, Cernicharo et al. 2013).

2.2.4 Performance Assessment

2.2.4.1 Validation Methods

The validation methods are described in detail in the Validation Document D06.

2.2.4.2 Uncertainties

As mentioned above, there are certain other plant characteristics that can interfere with the water signal at 970nm. This, and the radiometric uncertainties inherent in all satellite data (e.g. sensor noise, uncertainties through atmospheric and geometric correction) lead to uncertainties in the results of the algorithm. The algorithm itself does not calculate any uncertainty layer, meaning that results should be validated against in-situ data if possible.

2.2.5 Algorithm Implementation

2.2.5.1 Algorithm Availability

The algorithm is available within the EnMAP-Box, as a free and open-source plugin to QGIS, which is an open-source Geographical Information System (GIS). The two tools can be found at the following websites:

QGIS: https://qgis.org/de/site/forusers/download.html

EnMAP-Box: https://www.enmap.org/data_tools/enmapbox/

2.2.5.2 Input Data Access

The EnMAP-Box can process both PRISMA and EnMAP data. To access this data, it is necessary to write a short tender to ASI and DLR respectively, as the data is only available for research purposes and cannot be shared. More details on data access can be found here:

PRISMA: https://www.asi.it/en/earth-science/prisma/

EnMAP: https://www.enmap.org/data_access/

2.2.5.3 Output Data Access

Result data can be stored and accessed locally when using QGIS locally or it can be stored and accessed through the user account on the Food Security Explorer (https://foodsecurity-explorer.net) when using the QGIS application on the platform.

2.2.6 Significance Discussion

Plant water retrieval is an important tool, where remotely sensed data can support farm management decisions, as irrigation area is ever extending while freshwater resources are often becoming scarcer. This hyperspectral method of using the specific plant water absorption at 970nm allows to make use of a characteristic water feature that differentiates the water content from other plant characteristics, but also from soil water content or atmospheric water content, which has an absorption at 940nm.

3   Conclusion

3.1 Thermal Algorithms

For thermal drought indicators, we performed a sensitivity analysis of agricultural drought indices at 8-day and monthly scales, encompassing remote sensing indices such as ECOSTRESS ESI, SMAP SM, ESA SWI, STR, SDCI, and meteorological KBDI. In-situ measurements from the International Soil Moisture Network (ISMN) were employed as a reference to understand the sensitivity of these indices to soil moisture variability. Results reveal SMAP's greater performance, followed by SWI. STR correlates with SM but includes scattered values. ECOSTRESS ESI effectively captures the spatial nuances of local drought stress; however, it is limited by temporal sampling frequency, impeding the variability analysis at intra-monthly scales. No single index universally excels, underscoring the need for further refinement and combination of different indicators/approaches. Using a cross-sensor calibration strategy, we have demonstrated the complementarity of current thermal satellite missions for generating a high-resolution RS data-driven crop water stress index. These efforts have clearly indicated the potential benefits of future thermal missions (e.g., TRISHNA, SBG, LSTM) for enhanced drought monitoring in Africa.

3.2 Hyperspectral Algorithms

The hyperspectral algorithms utilized for ARIES to derive leaf area, leaf water content and canopy water content are based on validated scientific methods but are newly implemented for the African drought use case. The algorithms are mathematically sound and the results are being validated in the context of ARIES. The hyperspectral input data is available for research purposes and training data is not needed for the approaches, though further validation data would be advantageous to prove the stability of the approaches under different conditions. The algorithms are integrated in open-source tools, which in turn have been integrated on the Food Security Explorer to allow the Early Adopters to use the algorithms for different locations and time periods than covered in ARIES. More details on the prototype implementation can be found in D08 – Documentation of processors/toolboxes and software.

4 References

Bibliography Thermal

AghaKouchak, A., Farahmand, A., Melton, F.S., Teixeira, J., Anderson, M.C., Wardlow, B.D., Hain, C.R., 2015. Remote sensing of drought: Progress, challenges and opportunities. Reviews of Geophysics 53, 452–480.

Albergel, C., Rüdiger, C., Pellarin, T., Calvet, J.-C., Fritz, N., Froissard, F., Suquia, D., Petitpa, A., Piguet, B., Martin, E., 2008. From near-surface to root-zone soil moisture using an exponential filter: an assessment of the method based on in-situ observations and model simulations. Hydrol Earth Syst Sci 12, 1323–1337.

Alexander, M.E., 1990. Computer calculation of the Keetch-Byram Drought Index-programmers beware. Fire Management Notes 51, 23–25.

Al-Yaari, A., Wigneron, J.-P., Dorigo, W., Colliander, A., Pellarin, T., Hahn, S., Mialon, A., Richaume, P., Fernandez-Moran, R., Fan, L., 2019. Assessment and inter-comparison of recently developed/reprocessed microwave satellite soil moisture products using ISMN ground-based measurements. Remote Sens Environ 224, 289–303.

Bellvert, J., Jofre-Cekalovic, C., Pelechá, A., Mata, M. and Nieto, H. (2020). Feasibility of Using the Two-Source Energy Balance Model (TSEB) with Sentinel-2 and Sentinel-3 Images to Analyze the Spatio-Temporal Variability of Vine Water Status in a Vineyard. Remote Sensing, 12, 2299, https://doi.org/0.3390/rs12142299

Breiman, L. (1996). Bagging predictors. *Machine Learning*, *24*(2). https://doi.org/10.1007/bf00058655

Brown, E.K., Wang, J., Feng, Y., 2021. US wildfire potential: A historical view and future projection using high-resolution climate data. Environmental Research Letters 16, 034060.

Entekhabi, D., Njoku, E.G., O'neill, P.E., Kellogg, K.H., Crow, W.T., Edelstein, W.N., Entin, J.K., Goodman, S.D., Jackson, T.J., Johnson, J., 2010. The soil moisture active passive (SMAP) mission. Proceedings of the IEEE 98, 704–716.

Fisher, J.B., Lee, B., Purdy, A.J., Halverson, G.H., Dohlen, M.B., Cawse-Nicholson, K., Wang, A., Anderson, R.G., Aragon, B., Arain, M.A., 2020. ECOSTRESS: NASA's next generation mission to measure evapotranspiration from the international space station. Water Resour Res 56, e2019WR026058.

Gao, F., Kustas, W. P., & Anderson, M. C. (2012a). A Data Mining Approach for Sharpening Thermal Satellite Imagery over Land. *Remote Sensing*, *4*, 3287–3319. https://doi.org/10.3390/rs4113287

Gao, F., Kustas, W. P., & Anderson, M. C. (2012b). A Data Mining Approach for Sharpening Thermal Satellite Imagery over Land. *Remote Sensing*, *4*, 3287–3319. https://doi.org/10.3390/rs4113287

Gao, F., Kustas, W. P., & Anderson, M. C. (2012c). A Data Mining Approach for Sharpening Thermal Satellite Imagery over Land. *Remote Sensing 2012, Vol. 4, Pages 3287-3319*, *4*(11), 3287–3319. https://doi.org/10.3390/RS4113287

Guillevic, P., Göttsche, F., Nickeson, J., Hulley, G., Ghent, D., Yu, Y., Trigo, I., Hook, S., Sobrino, J. A., Remedios, J., Román, M., & Camacho, F. (2018). *Land Surface Temperature Product Validation Best Practice Protocol. Version 1.1*. https://doi.org/10.5067/doc/ceoswgcv/lpv/lst.001

Guzinski, R., & Nieto, H. (2019). Evaluating the feasibility of using Sentinel-2 and Sentinel-3 satellites for high-resolution evapotranspiration estimations. *Remote Sensing of Environment*, *221*, 157–172. https://doi.org/10.1016/J.RSE.2018.11.019

Guzinski, R., Nieto, H., Sandholt, I., & Karamitilios, G. (2020). Modelling High-Resolution Actual Evapotranspiration through Sentinel-2 and Sentinel-3 Data Fusion. *Remote Sensing*, *12*(9), 1433. https://doi.org/10.3390/RS12091433

Hadebe, S.T., Modi, A.T., Mabhaudhi, T., 2017. Drought tolerance and water use of cereal crops: A focus on sorghum as a food security crop in sub-Saharan Africa. J Agron Crop Sci 203, 177–191.

Idso, S.B.; Jackson, R.D.; Reginato, R.J. (1977). Remote-Sensing of Crop Yields. Science, 196, 19–25.

Jia, A., Hu, T., Mallick; Kanishka, 2024. Understanding the Sensitivity of Different Drought Indices to Soil Moisture Variations in Africa, in: 104th AMS Annual Meeting. AMS, Baltimore.

Jia, A., Liang, S., Wang, D., 2022. Generating a 2-km, all-sky, hourly land surface temperature product from Advanced Baseline Imager data. Remote Sens Environ 278. https://doi.org/10.1016/j.rse.2022.113105

Lagouarde, J. P., & Irvine, M. (2008). Directional anisotropy in thermal infrared measurements over Toulouse city centre during the CAPITOUL measurement campaigns: First results. *Meteorology and Atmospheric Physics*, *102*, 173–185. https://doi.org/10.1007/S00703-008-0325-4/METRICS

Otekunrin, Olutosin Ademola, Otekunrin, Oluwaseun Aramide, Sawicka, B., Ayinde, I.A., 2020. Three decades of fighting against hunger in Africa: Progress, challenges and opportunities. World Nutrition 11, 86–111. https://doi.org/10.26596/wn.202011386-111

Pérez-Planells, L., Niclòs, R., Puchades, J., Coll, C., Göttsche, F. M., Valiente, J. A., Valor, E., & Galve, J. M. (2021). Validation of sentinel-3 slstr land surface temperature retrieved by the operational product and comparison with explicitly emissivity-dependent algorithms. *Remote Sensing*, *13*(11). https://doi.org/10.3390/rs13112228

Rhee, J., Im, J., Carbone, G.J., 2010. Monitoring agricultural drought for arid and humid regions using multi-sensor remote sensing data. Remote Sens Environ 114, 2875–2887. https://doi.org/10.1016/j.rse.2010.07.005

Sanchez, J. M., Galve, J. M., Nieto, H., & Guzinski, R. (2024). Assessment of High-Resolution LST Derived from the Synergy of Sentinel-2 and Sentinel-3 in Agricultural Areas. *IEEE Journal of Selected Topics in Applied Earth Observations and Remote Sensing*, *17*, 916–928. https://doi.org/10.1109/JSTARS.2023.3335896

USER MANUAL FOR SEN-ET SNAP PLUGIN (V1.1.0). (2020). https://www.esa-sen4et.org/static/media/sen-et-user-manual-v1.1.0.2cd617fb322658397542.pdf

Yue, J., Tian, J., Tian, Q., Xu, K., Xu, N., 2019. Development of soil moisture indices from differences in water absorption between shortwave-infrared bands. ISPRS Journal of Photogrammetry and Remote Sensing 154, 216–230.

Bibliography Hyperspectral

Asner, G. P., Braswell, B. H., Schimel, D. S., & Wessman, C. A. (1998). Ecological research needs from multiangle remote sensing data. *Remote Sensing of Environment*, 63(2), 155–165. https://doi.org/10.1016/S0034-4257(97)00139-9

Ballaré C.L., Mazza C.A., Austin A.T., Pierik R. (2012) Canopy light and plant health. Plant Physiology, 160(1), 145-155. https://doi.org/10.1104/pp.112.200733

Baret, F. (2015). Canopy biophysical variables retrieval from the inversion of reflectance models. In P. S. Thenkabail (Ed.) *Land resources monitoring, modeling, and mapping with remote sensing* (1st ed., Vol. 2, 23–46). Boca Raton, FL: CRC Press

Berger, K., Atzberger, C., Danner, M., D'Urso, G., Mauser, W., Vuolo, F., & Hank, T. (2018). Evaluation of the PROSAIL model capabilities for future hyperspectral model environments: A review study. *Remote Sensing*,10(1), 85. https://doi.org/10.3390/rs10010085

Bréda, N. J. J. (2003). Ground-based measurements of leaf area index: A review of methods, instruments and current controversies. *Journal of Experimental Botany*, 54, 2403–2417. https://doi.org/10.1093/jxb/erg263

Bull, C. R. (1991). Wavelength selection for near-infrared reflectance moisture meters. Journal of Agricultural Engineering Research, 49, 113-125. https://doi.org/10.1016/0021-8634(91)80032-A

Cernicharo, J., Verger, A., & Camacho, F. (2013). Empirical and physical estimation of canopy water content from CHRIS/PROBA data. *Remote Sensing*, 5(10), 5265-5284. https://doi.org/10.3390/rs5105265

Chen, J. M. (2018). Remote sensing of leaf area index and clumping index. In Liang, S. (Ed.) *Comprehensive remote sensing*, 53–77. Oxford: Elsevier.

Clevers, J. G., Kooistra, L., & Schaepman, M. E. (2010). Estimating canopy water content using hyperspectral remote sensing data. *International Journal of Applied Earth Observation and Geoinformation*, 12(2), 119-125. https://doi.org/10.1016/j.jag.2010.01.007

Clevers, J. G., Kooistra, L., & Schaepman, M. E. (2008). Using spectral information from the NIR water absorption features for the retrieval of canopy water content. *International Journal of Applied Earth Observation and Geoinformation*, 10(3), 388-397. https://doi.org/10.1016/j.jag.2008.03.003

Fang, H., Baret, F., Plummer, S., & Schaepman-Strub, G. (2019). An overview of global leaf area index (LAI): Methods, products, validation, and applications. *Reviews of Geophysics*, 57, 739–799. https://doi.org/10.1029/2018RG000608

Féret, J. B., François, C., Asner, G. P., Gitelson, A. A., Martin, R. E., Bidel, L. P., Ustin, S.L., Le Maire, G. & Jacquemoud, S. (2008). PROSPECT-4 and 5: Advances in the leaf optical properties model separating photosynthetic pigments. *Remote sensing of environment*, 112(6), 3030-3043. https://doi.org/10.1016/j.rse.2008.02.012

Féret, J. B., Gitelson, A. A., Noble, S. D., & Jacquemoud, S. (2017). PROSPECT-D: Towards modeling leaf optical properties through a complete lifecycle. *Remote Sensing of Environment*, 193, 204-215. https://doi.org/10.1016/j.rse.2017.03.004

Féret J.B., Berger K., de Boissieu F. & Malenovský Z. 2021. PROSPECT-PRO for estimating content of nitrogen-containing leaf proteins and other carbon-based constituents. *Remote Sensing of Environment,* 252: 112173. https://doi.org/10.1016/j.rse.2020.112173

Fourty, T., Baret, F., Jacquemoud, S., Schmuck, G., & Verdebout, J. (1996). Optical properties of dry plant leaves with explicit description of their biochemical composition: Direct and inverse problems. *Remote Sensing of Environment*, 56, 104−117. https://doi.org/10.1016/0034-4257(95)00234-0

GCOS (2011). Systematic observation requirements for satellite-based products for climate, 2011 Update, Supplemental Details to the Satellite-Based Component of the Implementation Plan for the Global Observing System for Climate in Support of the UNFCCC (2011 Update). Retrieved from https://climate.esa.int/sites/default/files/gcos-154.pdf

Ghulam, A., Li, Z. L., Qin, Q., Yimit, H., & Wang, J. (2008). Estimating crop water stress with ETM+ NIR and SWIR data. *Agricultural and forest meteorology*, 148(11), 1679-1695. https://doi.org/10.1016/j.agrformet.2008.05.020

Goel, N. S. (1989). Inversion of canopy reflectance models for estimation of biophysical parameters from reflectance data. In Asrar G. (Ed.), *Theory and Applications of Optical Remote Sensing*, 205−251. New York: John Wiley & Sons.

Goel, N. S., & Thompson, R. L. (2000). A snapshot of canopy reflectance models and a universal model for the radiation regime. Remote Sensing Reviews,18, 197–225. https://doi.org/10.1080/02757250009532390

He, W., Yang, H., Pan, J., & Xu, P. (2012). Exploring optimal design of look-up table for PROSAIL model inversion with multi-angle MODIS data. *Land Surface Remote Sensing*. 8524, 327-339. https://doi.org/10.1117/12.977234

Houborg, R., Soegaard, H., & Boegh, E. (2007). Combining vegetation index and model inversion methods for the extraction of key vegetation biophysical parameters using Terra and Aqua MODIS reflectance data. *Remote Sensing of Environment*,106(1), 39–58. https://doi.org/10.1016/j.rse.2006.07.016

Huang, D., Knyazikhin, Y., Wang, W., Deering, D. W., Stenberg, P., Shabanov, N., Tan, B. & Myneni, R.B. (2008). Stochastic transport theory for investigating the three-dimensional canopy structure from space measurements. *Remote Sensing of Environment*, 112(1), 35–50. https://doi.org/10.1016/j.rse.2006.05.026

Jacquemoud, S., Ustin, S. L., Verdebout, J., Schmuck, G., Andreoli, G., & Hosgood, B. (1996). Estimating leaf biochemistry using the PROSPECT leaf optical properties model. *Remote Sensing of Environment*, 56, 194−202. https://doi.org/10.1016/0034-4257(95)00238-3

Jacquemoud, S., Verhoef, W., Baret, F., Bacour, C., Zarco-Tejada, P. J., Asner, G. P., François, C. & Ustin, S. L. (2009). PROSPECT+ SAIL models: A review of use for vegetation characterization. *Remote sensing of environment*, 113, 56 - 66. https://doi.org/10.1016/j.rse.2008.01.026.

Jacquemoud, S., & Baret, F. (1990). PROSPECT: A model of leaf optical properties spectra. *Remote sensing of environment, 34 (2), 75 – 91.* https://doi.org/10.1016/0034-4257(90)90100-Z.

Jakimow, B., Janz, A., Thiel, F., Okujeni, A., Hostert, P. & van der Linden, S. (2023) "EnMAP-Box: Imaging spectroscopy in QGIS," SoftwareX, vol. 23, p. 101507, 2023, doi: https://doi.org/10.1016/j.softx.2023.101507

Kuusk, A. (1991). The hot spot effect in plant canopy reflectance. In Myneni, R. B. & Ross, J. (Eds.), *Photon-vegetation interactions. Applications in optical remote sensing and plant ecology,* 139−159. Berlin: Springer Verlag.

Liang, S. (2004). Quantitative remote sensing of land surfaces. New York: John Wiley and Sons, Inc.

Lillesaeter, O. (1982) Spectral reflectance of partly transmitting leaves: Laboratory measurements and mathematical modeling. *Remote Sensing of Environment*. 12, 247–254. https://doi.org/10.1016/0034-4257(82)90057-8

Le Maire, G. & Francois, C. & Dufrêne, E. (2004). Towards universal broad leaf chlorophyll indices using PROSPECT simulated database and hyperspectral reflectance measurements. *Remote Sensing of Environment*. 89. 1-28. https://doi.org/10.1016/j.rse.2003.09.004

Newton, J. E., & Blackman, G. E. (1970). The penetration of solar radiation through leaf canopies of different structure. *Annals of Botany*, 34(2), 329-348. https://doi.org/10.1093/oxfordjournals.aob.a084373

Peñuelas, J., Filella, I., Biel, C., Serrano, L., & Savé, R. (1993). The reflectance at the 950–970 nm region as an indicator of plant water status. *International Journal of Remote Sensing*, *14*, 1887–1905. https://doi.org/10.1080/01431169308954010

Peñuelas, J., Pinol, J., Ogaya, R., Filella, I. (1997). Estimation of plant water concentration by the reflectance water index wi (r900/r970). *International Journal of Remote Sensing*, 18, 2869–2875. https://doi.org/10.1080/014311697217396

Pu, R., Ge, S., Kelly, M. & Gong, P. (2003). Spectral absorption features as indicators of water status in coast live oak (Quercus agrifolia) leaves. International Journal of Remote Sensing, 24(9), 1799–1810. https://doi.org/10.1080/01431160210155965

Quemada, C., Pérez-Escudero, J.M., Gonzalo, R., Ederra, I., Santesteban, L.G., Torres, N. & Iriarte J.C. (2021) Remote Sensing for Plant Water Content Monitoring: A Review. *Remote Sensing*. 13(11):2088. https://doi.org/10.3390/rs13112088

Rivera J.P.*,* Verrelst J., Leonenko G. & Moreno J. (2013) Multiple Cost Functions and Regularization Options for Improved Retrieval of Leaf Chlorophyll Content and LAI through Inversion of the PROSAIL Model. *Remote Sensing*. 2013, 5(7):3280-3304. https://doi.org/10.3390/rs5073280

Running, S.W., Gower, S. (1991). Forest-BGC, a general model of forest ecosystem processes for regional applications. Ii. Dynamic carbon allocation and nitrogen budgets. *Tree Physiology*, 9, 147–160. https://doi.org/10.1016/0304-3800(88)90112-3

Sims, D. A., & Gamon, J. A. (2003). Estimation of vegetation water content and photosynthetic tissue area from spectral reflectance: a comparison of indices based on liquid water and chlorophyll absorption features. *Remote sensing of environment*, 84(4), 526-537. https://doi.org/10.1016/S0034-4257(02)00151-7

Tagliabue, G., Boschetti, M., Bramati, G., Candiani, G., Colombo, R., Nutini, F., Pompilio, L., Rivera-Caicedo, J. P., Rossi, M., Rossini, M., Verrelst, J., & Panigada, C. (2022). Hybrid retrieval of crop traits from multi-temporal PRISMA hyperspectral imagery. *ISPRS Journal of Photogrammetry and Remote Sensing*, *187*, 362–377. https://doi.org/10.1016/j.isprsjprs.2022.03.014

Verhoef, W. (1984). Light scattering by leaf layers with application to canopy reflectance modeling: the SAIL model. *Remote Sensing of Environment*, 16, 125−141. https://doi.org/10.1016/0034-4257(84)90057-9

Verhoef, W. & Bach, H. (2003). Simulation of hyperspectral and directional radiance images using coupled biophysical and atmospheric radiative transfer models. *Remote Sensing of Environment*, 87, 23−41. https://doi.org/10.1016/S0034-4257(03)00143-3

Verhoef, W., & Bach, H. (2007). Coupled soil-leaf-canopy and atmosphere radiative transfer modeling to simulate hyperspectral multi-angular surface reflectance and TOA radiance data. *Remote Sensing of Environment*, 109, 166−182. https://doi.org/10.1016/j.rse.2006.12.013

Verhoef, W., Xiao, Q., Jia, L., & Su, Z. (2007). Unified optical-thermal four-stream radiative transfer theory for homogeneous vegetation canopies. *IEEE Transactions on Geoscience and Remote Sensing*, 45, 1808−1822. https://doi.org/10.1109/TGRS.2007.895844

Verhoef, W., Bach, H. (2012). Simulation of Sentinel-3 images by four stream surface atmosphere radiative transfer modeling in the optical and thermal domains. In: Remote sensing of environment, 120 (2012),197-207. https://doi.org/10.1016/j.rse.2011.10.034

Verrelst, J., Rivera, J. P., Leonenko, G., Alonso, L., & Moreno, J. (2014). Optimizing LUT-based RTM inversion for semiautomatic mappingof crop biophysical parameters from Sentinel-2and-3 data: Role of cost functions. *IEEE Transactions on Geoscience and Remote Sensing*,52(1), 257–269. https://doi.org/10.1109/TGRS.2013.2238242

Verrelst, J., Rivera, J. P., Veroustraete, F., Muñoz-Marí, J., Clevers, J. G. P. W., Camps-Valls, G., & Moreno, J. (2015). Experimental Sentinel-2 LAI estimation using parametric, non-parametric and physical retrieval methods—A comparison*. ISPRS Journal of Photogrammetry and Remote Sensing*,108, 260–272. https://doi.org/10.1016/j.isprsjprs.2015.04.013

Verrelst, J., Rivera-Caicedo, J. P., Reyes-Muñoz, P., Morata, M., Amin, E., Tagliabue, G., Panigada, C., Hank, T., & Berger, K. (2021). Mapping landscape canopy nitrogen content from space using PRISMA data. *ISPRS Journal of Photogrammetry and Remote Sensing*, *178*, 382–395. https://doi.org/10.1016/j.isprsjprs.2021.06.017

Vohland, M. (2008). Using imaging and non-imaging spectroradiometer data for the remote detection of vegetation water content. *Journal of Applied Remote Sensing*, 2(1), 023520. http://dx.doi.org/10.1117/1.2937937

Watson, D.J. (1947). Comparative physiological studies on the growth of field crops: I. Variation in net assimilation rate and leaf area between species and varieties and within and between years. *Annals of Botany. 11: 41–76.* https://doi.org/10.1093/oxfordjournals.aob.a083148.

Weiss, M., Troufleau, D., Baret, F., Chauki, H., Prévot, L., Olioso, A., Bruguier, N. & Brisson, N. (2001). Coupling canopy functioning and radiative transfer models for remote sensing data assimilation. *Agricultural and Forest Meteorology*, 108, 113−128. https://doi.org/10.1016/S0168-1923(01)00234-9

Wocher, M., Berger, K., Danner, M., Mauser, W., & Hank, T. (2018). Physically-Based Retrieval of Canopy Equivalent Water Thickness Using Hyperspectral Data. *Remote Sensing*, *10*, 1924. https://doi.org/10.3390/rs10121924

Zheng, G., & Moskal, L. M. (2009). Retrieving leaf area index (LAI) using remote sensing: Theories, methods and sensors. *Sensors*, 9(4), 2719–2745. https://doi.org/10.3390/s90402719

.